

In-Flight Studies of Aero-Optical Distortions

Around AAOL-BC

Matthew Kalensky¹, Stanislav Gordeyev², and Eric J. Jumper³
University of Notre Dame, Notre Dame, IN, 46556

The work described here seeks to characterize the aero-optical environment around the Airborne Aero-Optics Laboratory for Beam Control (AAOL-BC) at subsonic and transonic speeds. Wavefront measurements were taken at varying Mach numbers through both the naturally developing boundary layer on the aircraft surface and an artificially generated shear layer. Wavefront aberrations were quantified and delineated based on the convective speeds of aero-optical distortions. Upstream propagating sound waves, originating from the aircraft's engine, induced optical distortions identified in all collected wavefront data. The dominant frequency associated with these acoustical aberrations closely coincides with the engine's fan blade passing frequency. Speeds of the acoustical distortions were directly measured and found to agree with theoretical predictions. Levels of aero-optical distortions due to the downstream convecting boundary layer and shear layer were both found to increase with Mach number, consistent with existing scaling laws. Convective speeds and other properties associated with these fundamental flow-fields were also measured.

Nomenclature

M	= Mach Number
c	= Speed of sound
ρ	= Density at sea level
W	= Wavefront
OPD	= Optical Path Difference
R	= Autocorrelation matrix for POD
Φ	= POD mode
A	= POD temporal coefficient
λ_n	= POD eigenvalues
f	= Frequency
Λ	= Structure size
S	= Power spectral density
E	= Energy
χ	= Energy ratio
U_∞	= Freestream velocity
U_c	= Convective velocity
U_A	= Acoustic wave velocity
f_{BP}	= Blade pass frequency
n	= Harmonic number
ω	= Phase velocity
k_x	= Wavenumber

¹ Graduate Research Assistant, Department of Aerospace and Mech. Eng., Student AIAA Member

² Associate Professor, Department of Aerospace and Mech. Eng., AIAA Associate Fellow

³ Professor, Department of Aerospace and Mech. Eng., AIAA Fellow

I. Introduction

Directed energy, free-space communication, and high-resolution imaging systems amendable to aircraft implementation are desirable. The induced aero-optical effects associated with use of airborne optical systems are deleterious to the functionality of such systems. Therefore, in-flight characterization of “canonical” flows such as boundary layers and shear layers are necessary. In the past, hemispherical turrets are often used to maximize the field of regard of these systems. Consequently, the fluidic [1,2,3] and aero-optical [4,5,6] properties of turrets have been extensively studied in the last decade. However, in many applications, the optical system apparatuses such as steering and tracking components, can be installed internally. In this case, the turbulent boundary layer (TBL) formed over the aircraft fuselage is the primary source of optical distortions. This alternate system configuration assuages the nuisance of dealing with the harsh aero-optical environment and associated complexities of turrets. While generally less disturbing than the turbulent wake downstream of a non-aerodynamic bluff-body, aero-optical effects due to the boundary layer still cause undesired losses in laser beam intensity on target or high-speed imaging.

In addition to the aero-optical related effects in proximity of the aircraft, acoustical waves produced by the aircraft engines also affect the transmitted laser beam. These acoustical sources were observed and preliminarily studied from in-flight data acquired in a recent AAOL campaign [7]. It was shown that acoustical radiation in the form of sound waves emanating from the aircraft engine introduce appreciable spatial and temporal pressure/density variations, further distorting the outgoing laser beam.

The primary objective of AAOL is to provide an in-flight testing platform where aero-optics experiments can be performed under real conditions. AAOL campaigns have been an integral part of advancing current understanding of the aero-optical interactions associated with turrets [8,9]. It remains an instrumental program for acquisition of experimental data in realistic aero-optical flow-fields [4,5,6], as well as for studying effects of flow control devices on aero-optical performance. Today, the research breadth is extended again as AAOL is now employed to investigate beam control (AAOL-BC). Quantifying the aero-optical and aero-acoustical environment deepens the multifarious extent of beam control experimentation for which AAOL can be employed. Defining appropriate scaling laws, which is usually a result of physics-based modeling, allows the induced aero-optical effects to either be predicted for a different airborne testing platform or properly included in the preliminary system analysis. Therefore, adaptive optics, high-speed imaging, turbulence profiling tests, to name a few, can be conducted in confidence.

This paper investigates the aero-optical environment around AAOL-BC during in-flight testing of the two configurations discussed, at various subsonic and transonic speeds. The effects due to the boundary layer over the optical window and the engine-generated acoustical waves are experimentally investigated and represent the aero-optical and aero-acoustical environments associated with an internal component tracking system. Additionally, a perforated fence is attached to the fuselage of AAOL-BC to generate a close to canonical shear layer over the data acquisition window. This enables continuation of studying the effects that shear-layer dominated flows have on airborne laser systems. The results of these in-flight experimentally measured spatial and temporally resolved wavefronts at different Mach numbers are presented and analyzed. Scaling laws are proposed to make these findings serviceable for any in-flight optical system characterization.

II. Experimental Setups

The experiments were performed with the AAOL-BC. Succinctly, AAOL-BC consists of two Falcon-10 aircrafts flying in close formation nominally 50 m apart. One of the aircrafts, designated as the source aircraft, projects a 532 nm diverging laser beam onto a custom-designed optical quality window mounted on the second aircraft, referred to here as the laboratory aircraft. The window, shown in Fig. 1, left plot, has a clear aperture of 0.3048 m in diameter, with optical quality of less than $\lambda/10$. The window is mounted on a specially designed aluminum mount, meant to limit distortions to the attached boundary layer as fluid convects from the aircraft fuselage over the window.

To create a shear layer over the window, a porous fence is installed 0.35 m upstream of the acquisition window on the laboratory aircraft, as seen in Fig. 1, right plot. In previous laboratory studies, porous fences were shown to create a shear layer by slowing the flow downstream of the fence via turbulence-related total pressure losses [10]. The fence has a semi-circular shape with a radius of 0.152 m and is installed normal to the aircraft surface on a mounting bracket, 0.35 m upstream of the window center. The fence had a porosity coefficient of 0.4, defined as the area of open holes in the fence divided by the total fence area.

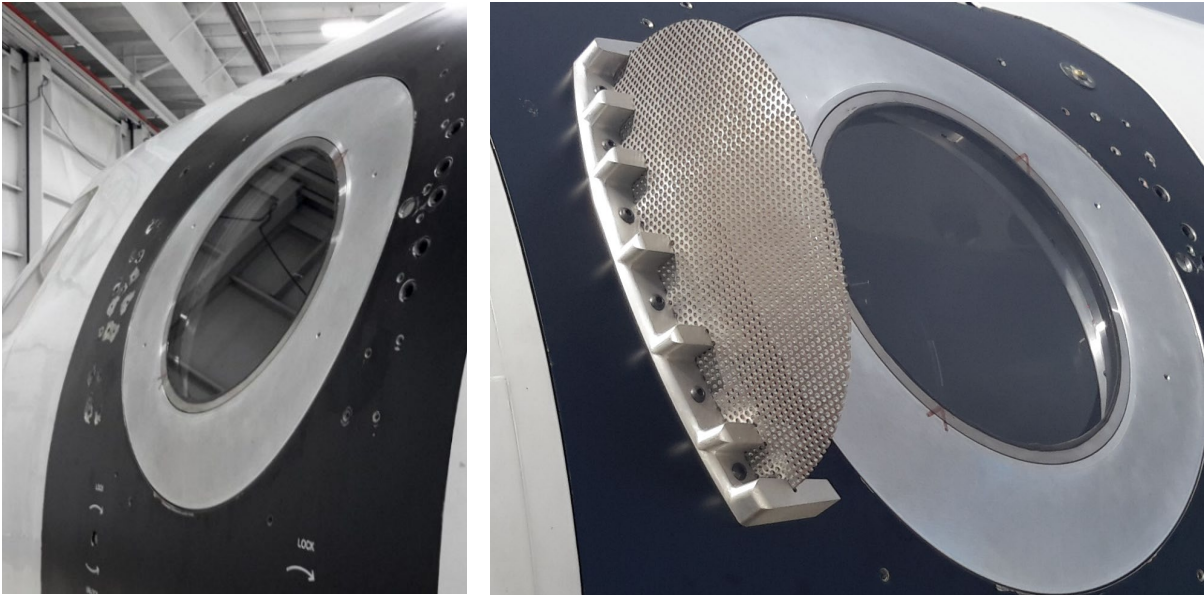


Figure 1. Left: Flat window for boundary layer tests. Right: Perforated plate installed in front of the flat window for shear layer studies

The laboratory aircraft was equipped with a beam stabilizing system, re-imaging optical components and a high-speed Shack-Hartmann wavefront sensor (SHWFS). The optical setup is illustrated in Fig. 2. Both planes were positioned such that the incoming beam is approximately normal to the flat window. To stabilize the incoming beam, a computer-controlled proportional feedback system was employed. The system consists of a tracking camera, a mirror controller, and an Aerotech gimbal with a flat mirror 0.3 m in diameter. The tracking camera collects images at 200 fps and computes relative image displacements in both horizontal and vertical directions. Using these computed displacements, the mirror controller commands motors on the gimbal to compensate for these angular differences.

After the incoming laser beam is stabilized, a Schmidt-Cassegrain telescope with a diameter of 203 mm and a central obscuration of 64 mm in diameter, coupled with several lenses, was used to contract an incoming circular 203 mm diameter beam to a collimated 16 mm diameter beam. This beam was then forwarded to the SHWFS. The SHWFS has a spatial resolution of 50x50 subapertures 0.3 mm in size, allowing the wavefront imposed on the beam to be measured with great accuracy. Wavefronts were acquired at 25 kHz producing 28,000 frames per collection. Flight static temperatures and pressures were also recorded during the flight.

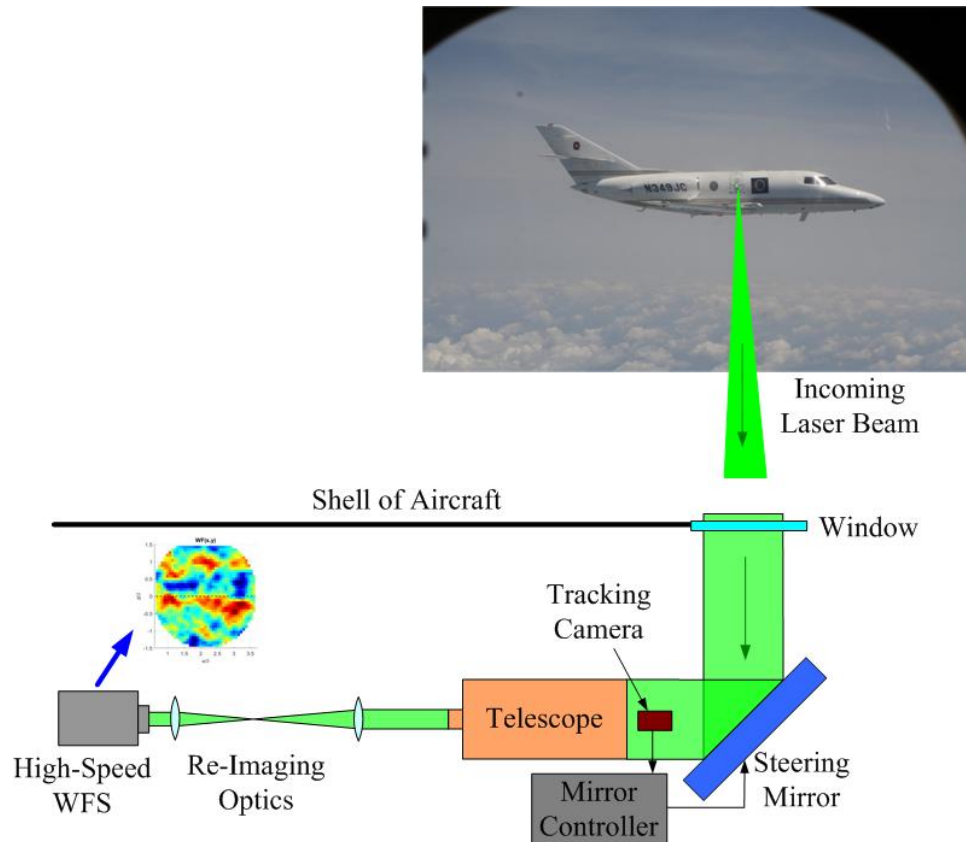


Figure 2. The optical setup and acquisition system on the AAOL-BC.

AAOL-BC's two Falcon-10 aircrafts can fly up to $M = 0.82$ at an altitude up to 12,000 m. At maximum engine throttle, the 32 blade Honeywell TFE-731-2-1C engine fan rotates at a speed of 11,502 rpm. During experiment, the percent of maximum throttle at each cruise Mach number was recorded allowing the blade pass frequency, f_{BP} , associated with each Mach number to be calculated. These results are presented in Table 1. Note that these calculations assume that the maximum cruise Mach number of the Falcon-10 jets corresponds to the manufacturer specified maximum rpm of the Honeywell engine fans at maximum throttle.

Table 1. Engine characteristics at various cruise Mach numbers.

Mach Number	Throttle (%)	Blade Pass Frequency [Hz]
0.4	77.4	4,748
0.5	81.3	4,987
0.6	91.5	5,613

During a separate flight campaign, three Pitot probe rakes were installed on a specially designed aluminum plate to measure the boundary layer properties over the data acquisition window location. Three rakes had 17 total pressure port locations each. This configuration is shown in Fig. 3, left plot, as well as described in Table 2. The position located 76 mm away from the aircraft fuselage also served as a 5-hole probe allowing local flow angle to be determined. The three rakes were separated by 75 mm in the spanwise direction to check for uniformity. The middle rake was centered in the vertical direction over the aluminum mounting insert and two more rakes were placed above and below. This configuration can be seen in Fig. 3, right plot. For each rake, all ports were located along a straight line, normal to the aircraft surface. The streamwise coordinate for all ports was the same, 4 m from the nose of the aircraft or 105 mm upstream of the aluminum insert's center, seen in Fig. 3, left plot, and marked as a gray circle in Fig. 3, right plot. This was done so the data was collected normal to the freestream flow, as shown by the yellow line in Fig. 3, right plot.

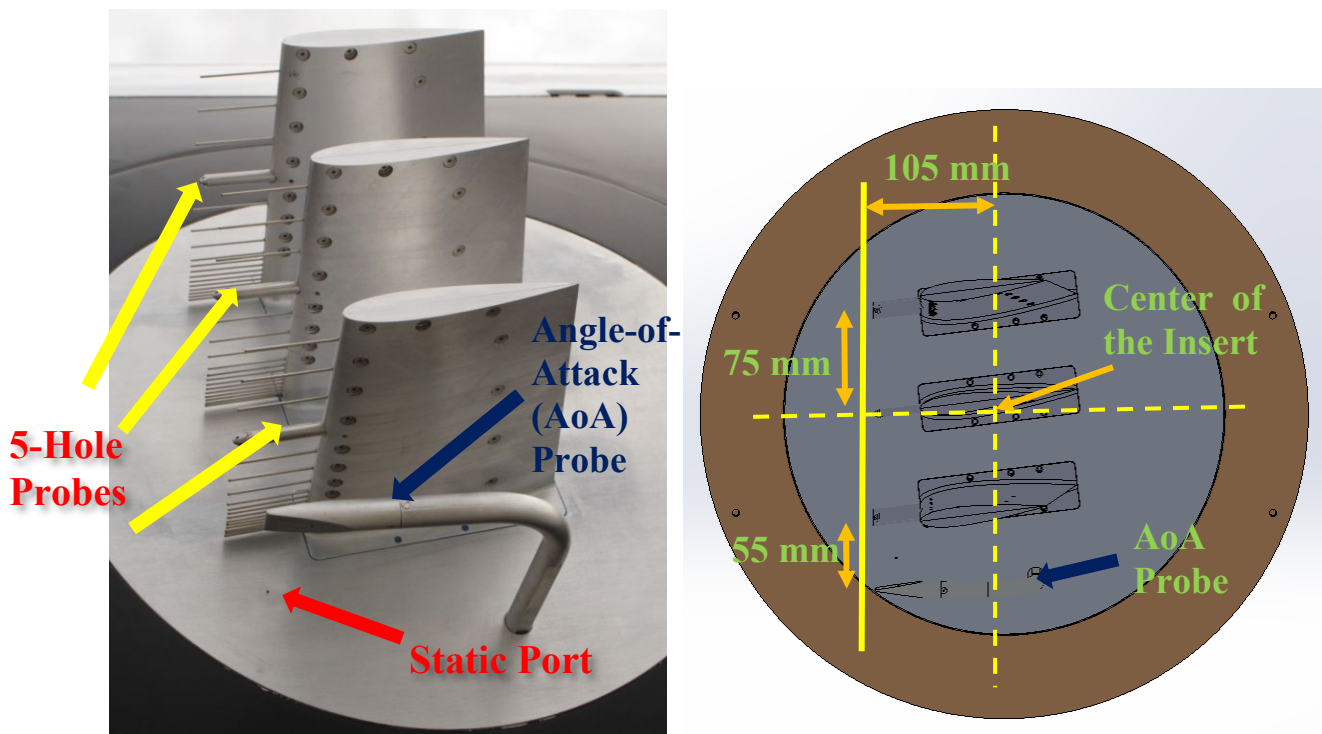


Figure 3. Left: Three rakes plus the Angle-of-Attack probe mounted to the aircraft. Right: Top view, with proper dimensions, of the rake assembly mounted on the aluminum insert.

The instrumentation for the boundary layer rakes and 5-hole probes consisted of one ZOC33 Scanivalve unit. The AoA probe used two Setra Model 205-2 (0-25 PSI) absolute pressure sensors and a Setra Model 239 (± 2 PSID) differential sensor. The Scanivalve unit consisted of eight 5 PSI differential pressure sensor modules with eight channels each, giving 64 total available channels. Each of the eight modules were referenced to the static port. The acquisition system for the Scanivalve unit was a DSM 3400 model system. Each rake consisted of 17 total pressure ports and 4 opposed ports on the 5-hole probe. Altogether, 63 channels on the Scanivalve system were used. The data from these sensors were acquired using a Data Translation DT9836 acquisition board.

Data from the two acquisition systems were acquired concurrently, though the two systems were not directly synchronized. The AoA probe acquired data with the DT9836 acquisition board

for 10 seconds at a rate of 1 kHz. The Scanivalve system acquires each channel sequentially with a prescribed delay of 100 microseconds between each sample. Therefore, the actual sample rate of the Scanivalve unit was 156.25 Hz. A total of 2000 samples per channel were obtained and averaged over time.

Table 2. Locations of total and 5-hole probes away from the aircraft wall.

Probe Type	Location from wall (mm)
Total pressure port	2.5 4.0 6.5 8.5 11.0 14.0 17.5 20.5 24.0 28.0 36.0 46.5 59.5 76.0 98.0 117.0 136.0
5-hole probe	76.0

The velocity data were collected at an altitude of 6096 m and Mach numbers of 0.5, 0.6 and 0.72. Ambient flight conditions during the experiments are given in Table 3. All Mach numbers were within ± 0.02 during the data collection. The error in the estimated aircraft angle of attack was approximately ± 0.5 degrees.

Table 3. Flight conditions for BL investigation using Pitot rakes.

Altitudes (m)	Mach Numbers	Freestream Pressure (kPa)	Freestream Temperature (C)	Estimated aircraft angle of attack (deg)
6,096 (20,000 ft)	0.5, 0.6, 0.72	48.3	-20	M=0.5: 4.5 ± 0.5 M=0.6, 0.72: 3 ± 0.5

Streamwise velocities were calculated for each pitot rake using the isentropic flow relation between pressure and velocity. Both the azimuthal velocity and the wall-normal velocity angles were calculated at each 5-hole probe location using the calibration curve.

III. Wavefront Data Analysis

The Optical Path Difference (OPD) is defined as the conjugate of the wavefront,

$$OPD(x, y, t) = -W(x, y, t) \quad (1)$$

The root mean square (RMS) of the OPD in space is a measure of the time-dependent wavefront's departure from planarity, as shown in Eq. 2.

$$OPD_{RMS}(t) = \left\langle OPD(x, y, t)^2 \right\rangle_{x,y} \quad (2)$$

Here the brackets denote averaging over the spatial coordinates. The OPD_{RMS} refers to the average RMS of the OPD in time and elicits the average degree of wavefront aberrations. OPD_{RMS} is the most common metric to quantify the degree of distortion associated with an aero-optical environment,

$$OPD_{RMS} = \overline{OPD_{RMS}(t)} \quad (3)$$

Proper Orthogonal Decomposition (POD) is a method that seeks a low dimensional modal decomposition of an entire data set [11]. The technique has gained popularity with fluid mechanists because the prevalent spatial features of a fluid environment can often be captured with just a few modes. Only a brief description of the procedure will be provided here but a thorough explanation can be found in [11], for instance. POD allows the decomposition of measured wavefronts, W , into orthogonal spatial modes, ϕ_i , and temporal coefficients, a_i , as seen in Eq. 4.

$$W(x, y, t) = \sum_i a_i(t) \phi_i(x, y) \quad (4)$$

The modes are found by solving the eigenvalue problem, described in Eq. 5.

$$\int R(x, y, x', y') \phi_i(x', y') dx' dy' = \lambda_i \phi_i(x, y) \quad (5)$$

Here $R(x, y, x', y') = \overline{W(x, y, t)W(x', y', t)}$ is the two-point spatial correlation matrix. The temporal coefficients are found by taking the inner product of the modes with the wavefronts, as shown in Eq. 6.

$$a_i(t) = \int W(x, y, t) \phi_i(x, y) dx dy \quad (6)$$

The amount of optical “energy” in each mode is given by its eigenvalue, which can be computed either by solving Eq. 5 or from the temporal coefficients, given by Eq. 7.

$$\lambda_n = \overline{a_n^2(t)} \quad (7)$$

POD finds the optimal basis set of orthogonal spatial modes for a given set of data [11]. For this study, it was used to identify and study various wavefront modes and determine their comparative importance to other aero-optic distortions. Specific modes can easily be isolated and removed from the model data set using POD. The orthogonality requirement ensures that the absence of these modes does not compromise the physicality of the remaining modes. This technique has increased utility if the user has insight into the form of the spatial feature (or mode) of interest.

To investigate the convective speed and propagation direction of various optically-aberrating flow components, a dispersion analysis was also applied to one-dimensional “slices”, i.e. along $y=\text{const}$ line of the wavefront data. The dispersion analysis is effective at studying upstream-moving acoustic and downstream convecting, boundary- or shear-layer related optical disturbances. This approach transforms a two-dimensional data set (x (streamwise), and t (time)) into the wavenumber-frequency domain by a two-dimensional Fourier Transform, described by Eq. 8.

$$W(x, t) = \iint \widehat{W}(k_x, \omega) \exp[i(k_x x - \omega t)] dk_x d\omega \quad (8)$$

The convective velocity for each wavenumber can be calculated using the dispersion relation as shown in Eq. 9 [12].

$$\omega(k_x) = k_x U_c(k_x) \quad (9)$$

IV. Results and Discussion

a. Boundary Layer Profiles

Streamwise velocity profiles for different rake locations taken at an altitude of 6,096 m for different Mach numbers are shown in Fig. 4. For all Mach numbers, the velocity profiles generated from the bottom rake are illustrative of a typical attached TBL profile. The TBL thickness from the bottom rake was approximately 0.04 m. At other locations, the velocity profiles appear to have

a velocity deficit, effectively thickening the boundary layer. For the top rake profile at $M = 0.5$, the velocity deficit extends up to 0.1 m away from the wall. Similar deficits were observed for the top and middle rake profiles at $M = 0.6$, as well as for the middle rake profile at $M = 0.72$, as seen in Fig. 4. One possible explanation for these velocity deficits is the presence of a vortical structure, thought to originate from the wiper shield at the bottom of the pilots' cockpit window. The transition of the vortical structure from the top rake at $M = 0.5$ to the middle rake at $M = 0.72$ is due to the varying aircraft angle of attack associated with flying at different speeds. At lower speeds, the angle of attack of the aircraft is higher to maintain adequate lift. Here, the vortical structure is expected to move upward toward the top rake. When the speed is increased, the angle of attack is decreased, and the structure moves downward toward the bottom rake. Thus, due to the increased turbulence intensity associated with the presence of this vortical structure, the boundary layer over the rake locations is expected to deviate from a canonical description.

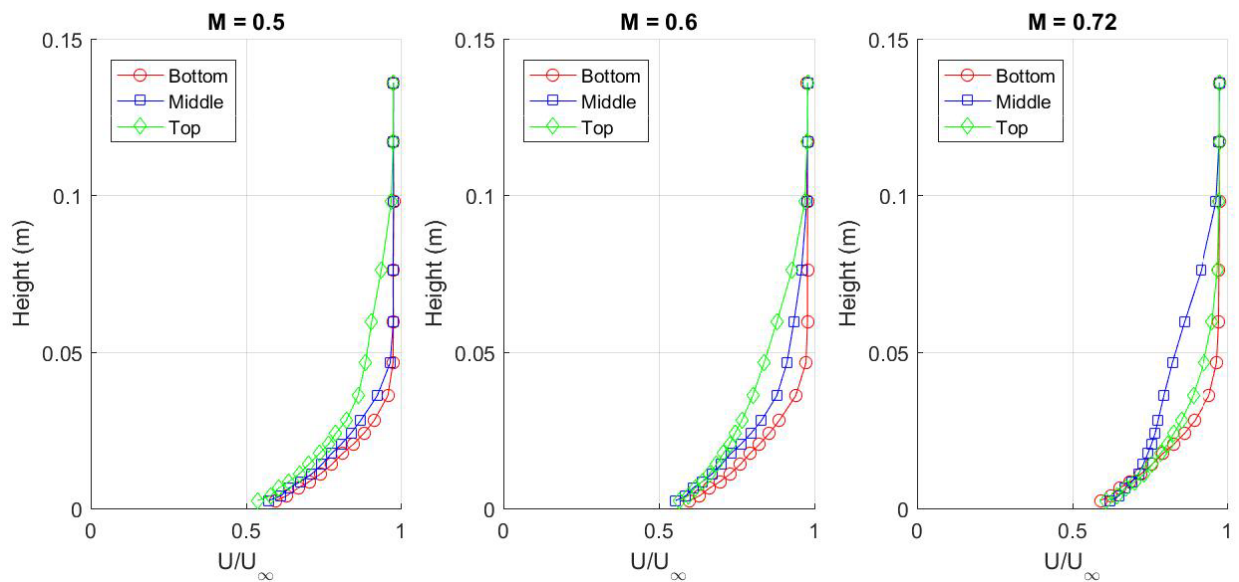


Figure 4. Streamwise velocity profiles for different rakes for the altitude of 6,096 m.

b. Boundary Layer Wavefront Analysis

Representative wavefronts for $M = 0.4$ are presented in Fig. 5. The wavefronts show small-scale spatially scattered optical distortions traveling in the direction of the flow, typical of a TBL. Upon closer inspection, the wavefront time series seems to also contain upstream traveling spanwise-uniform, periodic structures indicated by the arrows in Fig. 5.

These upstream traveling optical structures in AAOL wavefront data were discovered and investigated in [7]. They were shown to result from acoustic waves emanating from the aircraft's jet engine, located approximately 4.4 m downstream of the data acquisition window. The aperture-averaged power spectral densities were computed for the wavefront time series at each Mach number. The resultant plots can be seen in Fig. 6. For each of the cases presented below, there is a clear dominant peak in the spectra related to the f_{BP} calculated above. The secondary peaks are associated with the harmonic. As previously alluded to, the f_{BP} calculation assumes that the maximum cruise Mach number of the Falcon-10 jets corresponds to the manufacturer specified maximum rpm of the Honeywell engine fans. The consistent deviation of the acoustic peaks in the experimental results from the expected values is likely attributed to an overprediction of the maximum rpm of the engine fans.

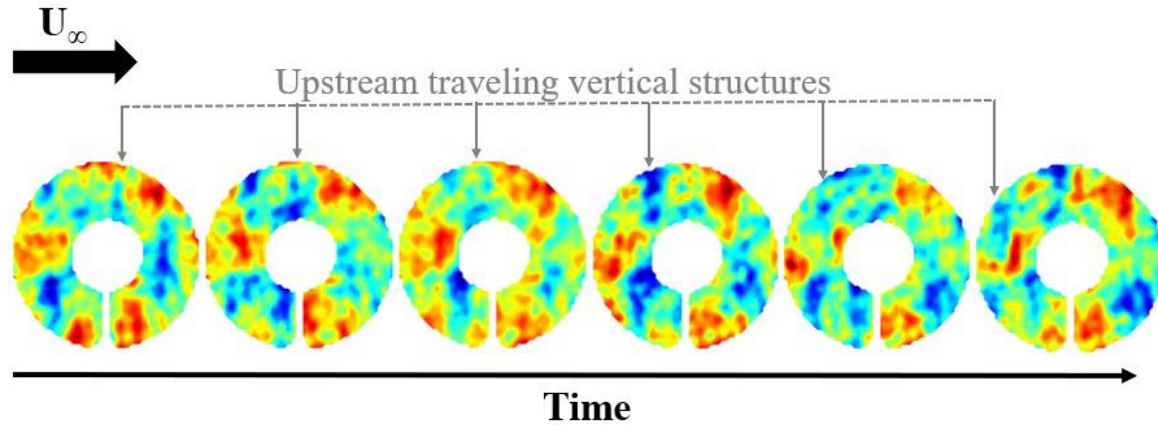


Figure 5. Consecutive wavefront time series for the boundary layer case.

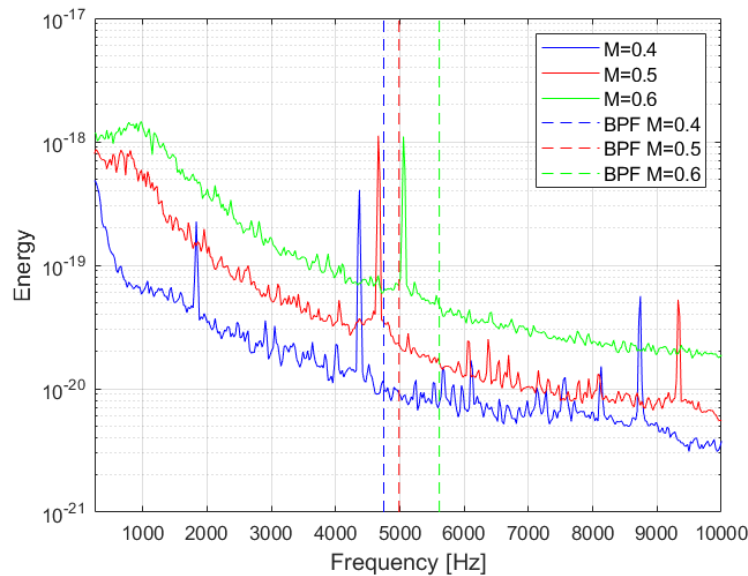


Figure 6. Wavefront spectra for the boundary layer case for various Mach numbers.

POD analysis was employed to further study and separate the upstream traveling acoustic disturbances from the boundary layer associated wavefront aberrations. The computed POD for the $M = 0.6$ wavefront time series can be seen in Fig. 7. While most modes do not have any directional organization, and correspond to the turbulent boundary layer, Modes 12, 13 and 14 show pronounced vertical striations indicative of the acoustic waves.

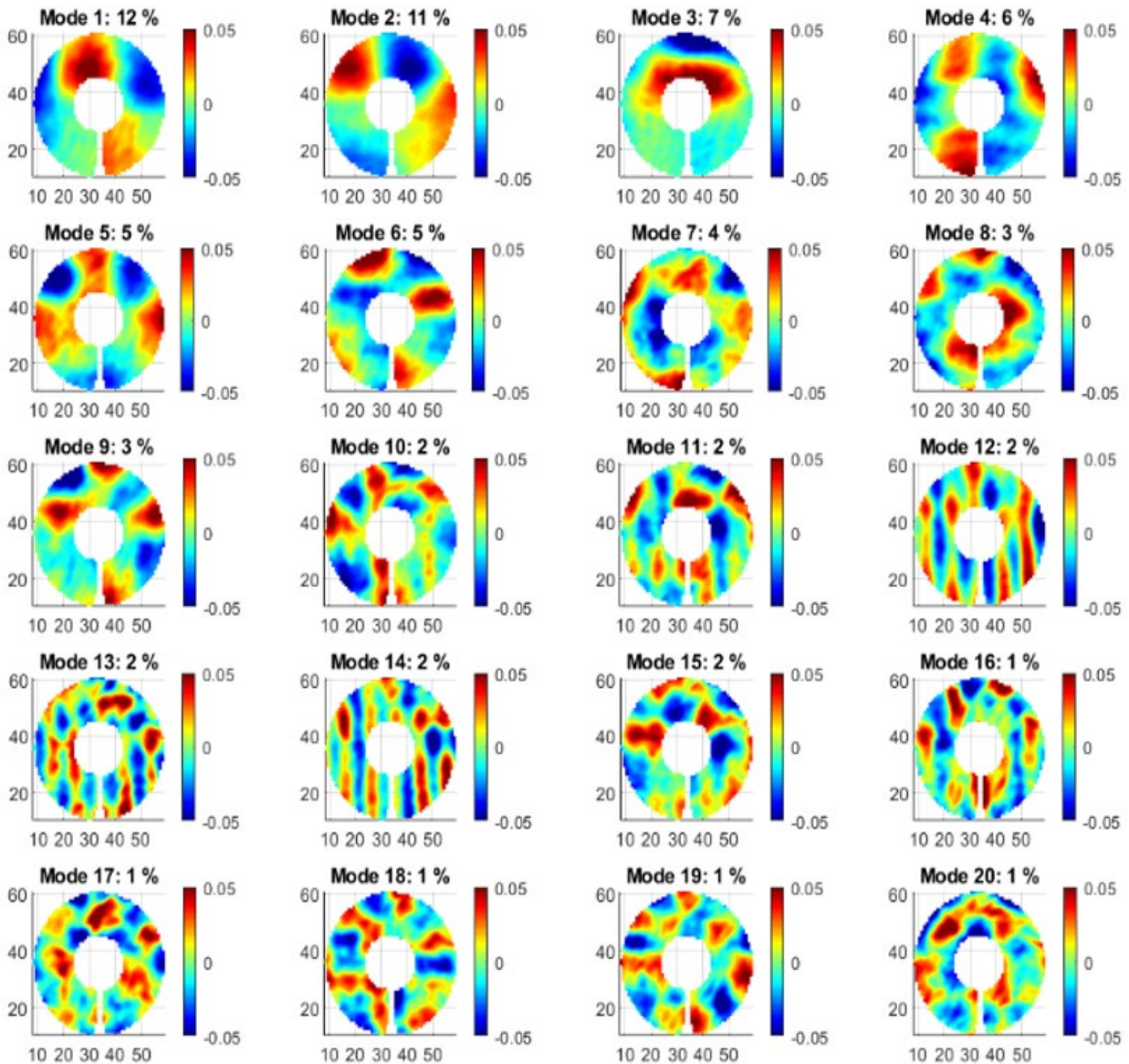


Figure 7. POD analysis for the boundary layer, $M = 0.5$, experiment.

In order to systematically diagnose which modes are associated with acoustic contamination, the power spectral densities for the POD time coefficients associated with each mode were calculated. The spectral plots were pre-multiplied by frequency and plotted on a log-linear scale to better illustrate the energy containing components of each mode. The results for the dominant modes 1 through 3 and acoustically related modes 12 through 14 can be seen in Figs. 8 and 9, respectively. The utility of this procedure becomes apparent. Modes 1 to 3, the highest energy containing modes, are absent of any appreciable acoustic related peak. However, the energies associated with modes 12 to 14 are almost entirely contained from the spectral peak at the f_{BP} of the engine fans.

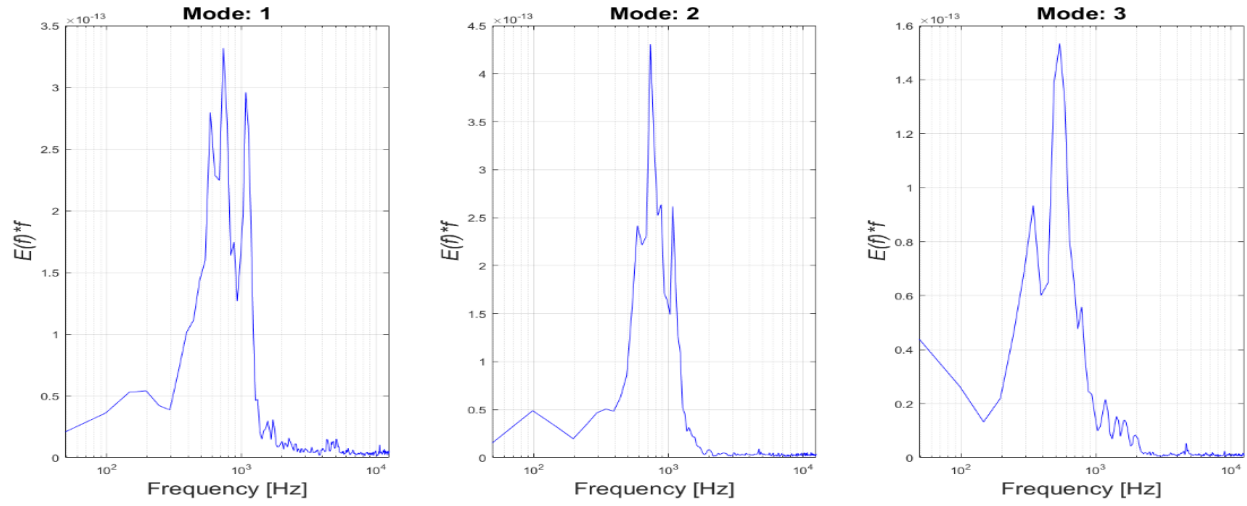


Figure 8. Pre-multiplied power spectra for modes 1,2 and 3 for Mach 0.5 boundary layer data.

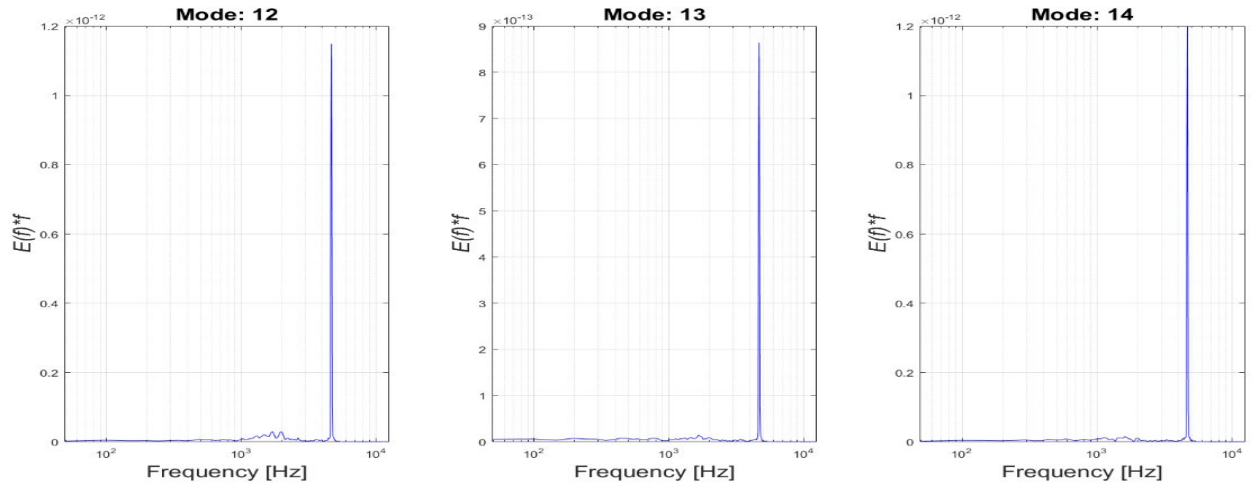


Figure 9. Pre-multiplied power spectra for modes 12, 13 and 14 for Mach 0.5 boundary layer data.

To more quantitatively delineate between boundary layer and acoustic originating modes, a bandpass filter, $[f_1 f_2]$ with a width of $f_2 - f_1 = 100$ Hz was applied around the known acoustic peak for each Mach number. The energy within this range and the energy over the entire frequency domain was calculated for each POD mode. The ratio between these calculated energies, χ represents a measure for quantifying the acoustical energy present in each mode, as defined by Eq. 8.

$$\chi = \frac{\int_{f_1}^{f_2} \left[\int_{-\infty}^{\infty} x(t) e^{-i2\pi f t} dt \right]^2 df}{\int_{-\infty}^{\infty} \left[\int_{-\infty}^{\infty} x(t) e^{-i2\pi f t} dt \right]^2 df} \quad (10)$$

A plot of χ versus mode number for the $M = 0.6$ case can be seen in Fig. 10. For certain modes, such as mode 22 and 23, most (greater than 50%) of the energy is contained within the acoustic related band of the spectrum. A threshold was introduced that dictates whether a mode imparts significant enough acoustical contamination necessitating its removal. For the $M = 0.6$ data, a threshold of $\chi = 0.2$ was imposed, as illustrated by the red dotted line in Fig. 10. Any mode with an acoustic energy ratio value greater than 0.2 was identified as an acoustic mode and was removed

from the original data. Therefore, the reconstructed data set in the absence of these acoustically dominant modes will be predominantly boundary layer related distortions. It is important to note that in some form, the acoustic effect is embedded in all the POD modes. While the threshold provides a measure of which POD modes contain considerable acoustic induced distortions, it is unrealistic to completely isolate and remove all acoustic contamination from the original wavefronts.

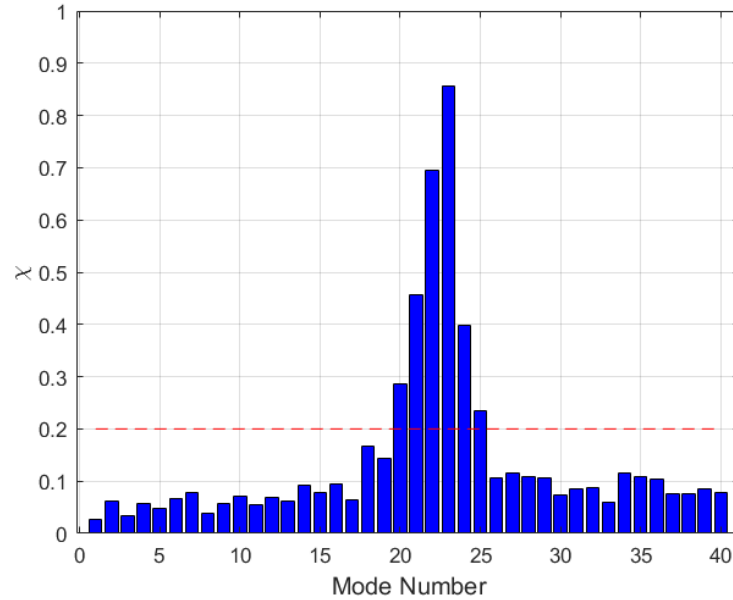


Figure 10. χ v. POD mode number for M=0.6 boundary layer experiment. Red line represents a threshold to identify acoustically-dominant POD modes.

The dispersion analysis method, examines wavefront data in the frequency versus the streamwise spatial wavenumber space. The utility of this approach is that the ranges of positive and negative frequencies correspond to the downstream and upstream moving structures, respectively. Fig. 11 illustrates the dispersion analysis of the original wavefront time series and the reconstructed data set after POD was applied to remove the acoustic effect for the M = 0.6 case. In Fig. 11, left plot, two distinct branches can be seen. One broad-band branch is located in the upper, positive-frequency region, corresponding to downstream-convecting structures inside the boundary layer. Most of the spectral energy is associated with this boundary layer related branch. Circles indicate the local peaks in the spectrum. In tunnel studies, the convective speed of aero-optical subsonic boundary layer structures was found to be approximately 0.85 of the freestream speed [12]. A solid line, corresponding to this convective speed is also plotted in Fig. 11. This line agrees well with the locations of the local spectral maxima, indicating that the aero-optical structures of the in-flight boundary layer convect at this speed.

Another, much weaker branch can be observed in the lower, negative-frequency region, related to the upstream traveling acoustical waves originating from the aircraft engine. The branch has one distinct peak at $(f, k_x/(2\pi)) \approx (-5,000 \text{ Hz}, 35 \text{ 1/m})$, corresponding to the blade pass frequency, f_{BP} , of the engine fan, and the related wavenumber. The dashed line represents the expected speed of the optical distortions due to the acoustic waves, $a - U_\infty$, where a is the freestream speed of sound, and it agrees well with the branch orientation.

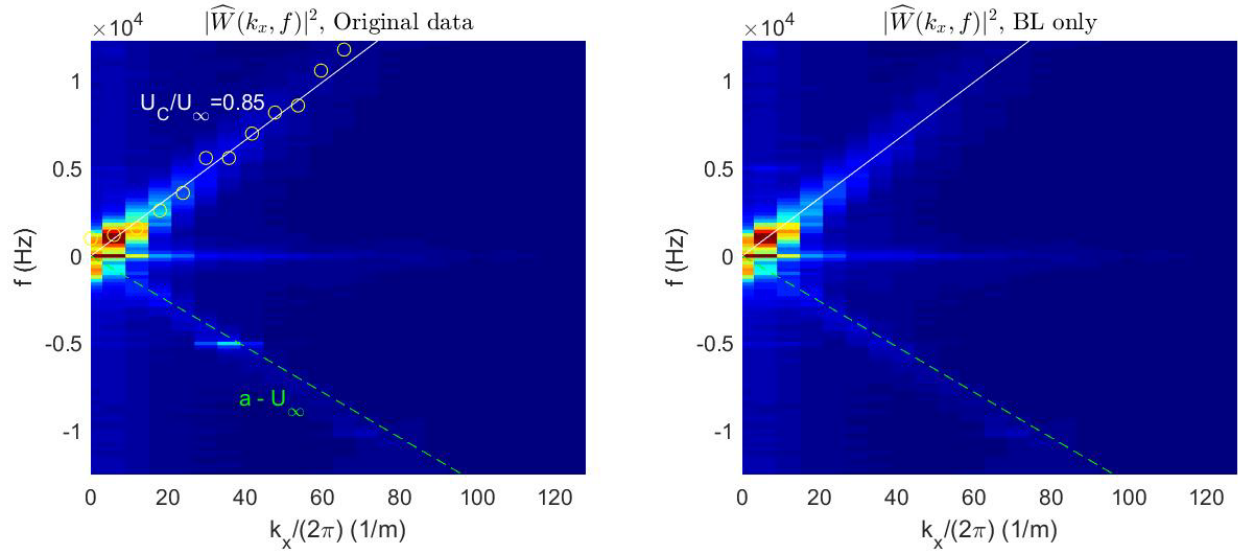


Figure 11. Two-dimensional Fourier transform, $|\widehat{W}(k_x, f)|^2$, for $M = 0.6$, applied to the original wavefront data (left) and the reconstructed set, using only boundary layer POD modes (right). Different convective speeds are indicated by solid and dashed lines.

To validate that the χ -threshold approach, applied to POD modes, successfully eliminates most of the optical aberrations imposed by the upstream propagating sound waves, a wavefront time series were reconstructed with only the modes whose energy ratio was greater than the threshold value, indicated in Fig. 10. The results of the dispersion analysis, applied to the reconstructed wavefront data are presented in Fig. 11, right plot. The main peak in the acoustic branch is eliminated, while the upper, boundary layer branch is unchanged. The acoustic related wavefronts were also reconstructed using only POD modes, whose energy ratio were greater than the threshold.

The described POD-based procedure to eliminate acoustically related effects was applied for each cruise Mach number dataset in the TBL analysis. The boundary layer and acoustically related components of OPD_{RMS} were computed and plots of these results as a function of Mach number can be seen in Fig. 12. The acoustical component of OPD_{RMS} is approximately $0.02 \mu\text{m}$ and largely independent of the aircraft speed, as the engine throttle percentage was about the same. Thus, the effect of engine noise imparted on the optical data is approximately the same at each cruise Mach number.

As seen in Fig. 12, right plot, the boundary layer component of the aero-optical distortions increases with the Mach number. In Ref. 12, aero-optical distortions of a canonical turbulent boundary layer were extensively studied and a model for the TBL induced aberrations was developed. The model predicts that at subsonic speeds, OPD_{RMS} is proportional to the boundary layer thickness, δ , and a square of the incoming Mach number, $OPD_{RMS} \sim \rho M^2$. Using $\delta \sim 0.05 \text{ m}$ as the boundary layer thickness estimate based on the Pitot rakes studies discussed earlier, the theoretical prediction of OPD_{RMS} for a canonical TBL with the same thickness is also presented in Fig. 12, right plot. While the model qualitatively predicts the increase in OPD_{RMS} with Mach number, the boundary layer present around AAOL-BC induces more than twice of the theoretical prediction. This indicates that the boundary layer on the aircraft surface is not canonical. The deviation from a canonical description is most certainly due to the presence of the vortical structure

over the window, as described earlier. This structure introduces additional turbulence and consequently, additional aero-optical distortions.

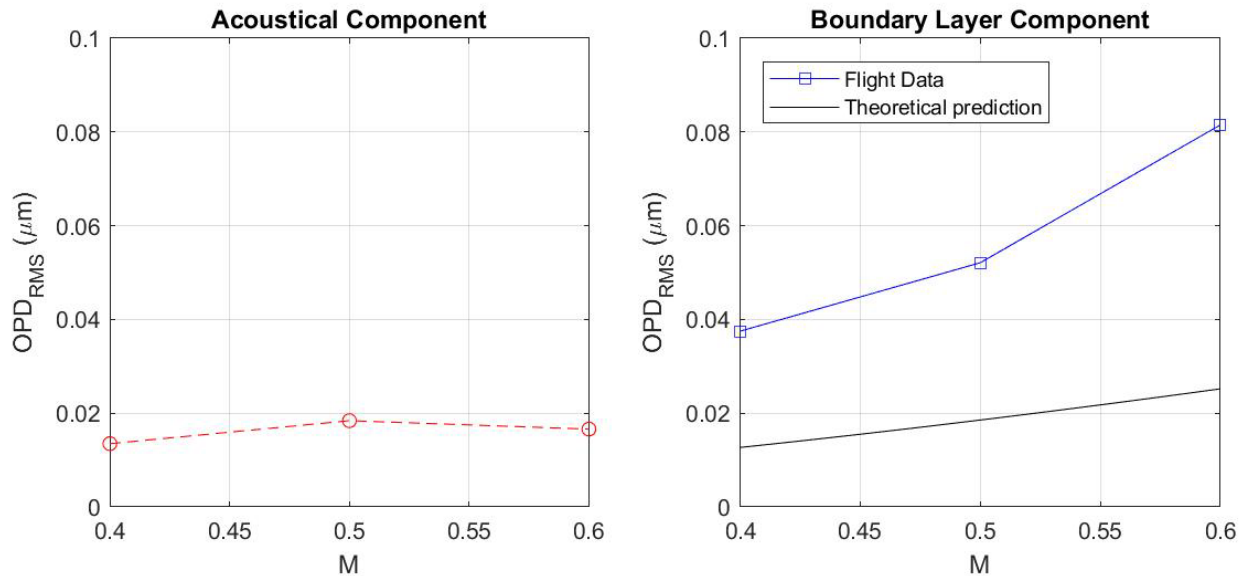


Figure 12. OPD_{RMS} v. Mach number for the acoustical component (left) and the boundary layer component (right). A theoretical prediction for a canonical boundary layer, based on the estimated BL thickness is also presented in the right plot.

In addition to quantifying the overall level of acoustically related distortions, the acoustic wave structure size, Λ_A , as well as the acoustic wave convective velocity, U_A , can also be directly measured. Using the POD mode with the greatest acoustic energy ratio value for each Mach number case, a normalized spatial correlation function was calculated for varying streamwise separations. The results can be seen in Fig. 13. The acoustic wave structure size for each Mach number is defined as the location of the first positive peak in the correlation function. Using the frequency value of the main peak, f_{BP} , identified in the spectra, the convective velocity of the acoustic waves, U_A can be calculated as $U_A = \Lambda_A f_{BP}$. The experimental results, as well as the theoretical prediction, $U_{A,Theory} = a \cdot U_\infty$, can be found in Table 4. The theoretical and experimental values are in close, within 4%, agreement with each other.

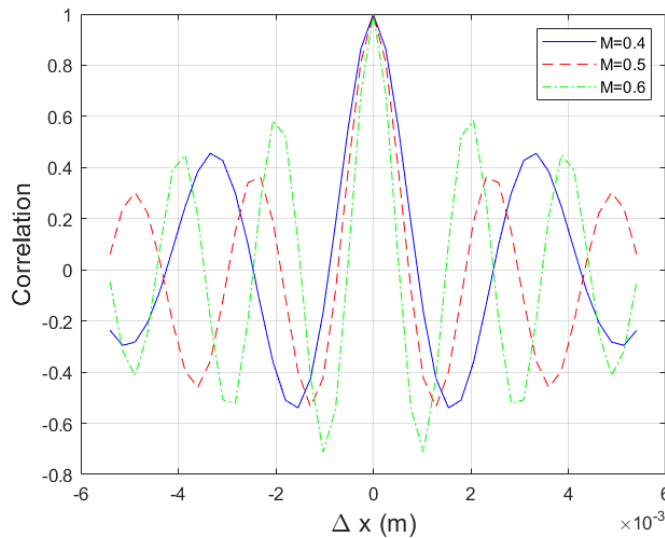


Figure 13. Normalized spatial correlations for different streamwise separation for the acoustic POD modes.

Table 4. Acoustic wave characteristics for varying Mach numbers.

Mach Number	Acoustic Wave Frequency (Hz)	Acoustic Wavelength, Λ_A (m)	Theoretical Convective Acoustic Velocity, $U_{A,Theory}$ (m/s)	Calculated Convective Acoustic Velocity, U_A (m/s)
0.4	4346	0.00334±0.00013	192	184
0.5	4687	0.00257±0.00013	160	153
0.6	5078	0.00206±0.00013	128	133

c. Shear Layer Wavefront Analysis

The porous fence, shown in Fig. 1, right plot, introduced a velocity mismatch by slowing the flow downstream of the fence, which formed a shear layer over the data acquisition window. The representative wavefronts collected for the $M = 0.5$ case are shown in Fig. 14. The large, periodic optical distortions are clearly observed. The structures are also nearly uniform in the vertical direction indicating that the porous fence was functioning as anticipated. These distortions are due to localized regions of lower pressure (and consequently, lower density) inside the vortical structures. The regular vortical structures, characteristic of shear layers, are caused by an inflection instability mechanism [13].

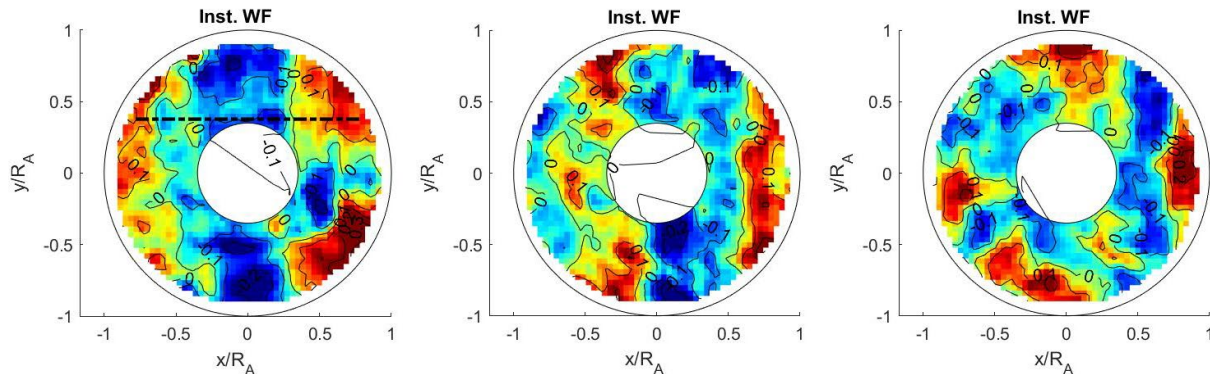


Figure 14. Representative wavefronts collected downstream of the porous fence. Spatial coordinates are normalized by the beam radius, $R_A = 0.1$ m. Incoming $M = 0.5$, flow goes from left to right. One-dimensional wavefronts were extracted for additional analysis along a dashed-dotted line, shown in the left plot.

To determine the size of the large-scale structures in the streamwise direction, one-dimensional slices of the wavefronts, $W_1(x,t) = W(x, y = \text{const}, t)$, were extracted along the black dashed-dotted line, as shown in Fig. 14. Similar to the analysis of the acoustic wavefront data, normalized correlations for different spatial separations, Δx , and for various Mach numbers were computed and are presented in Fig. 15. For the $M = 0.5$ and 0.6 cases, the pseudo-periodic nature of the optical distortions results in large negative correlations (-0.6) for $\Delta x \sim 0.06$ m, and large positive correlations (0.3) for separations of $\Delta x \sim 0.13$ m. As like before, the streamwise structure size, Λ_{SL} , was calculated by using the location of the first positive peak of the correlation function. The shear layer structure size was measured be $\Lambda = 0.133$ m for the $M = 0.5$ case and $\Lambda = 0.137$ m for the $M = 0.6$ case. At $M = 0.7$, the correlation was found to be qualitatively the same, but with smaller values for the negative and the positive correlations (-0.4 and 0.12 , respectively). This

indicates that the shear layer environment is less organized at this speed. Here, the structure size was found to be $\Lambda = 0.14$ m.

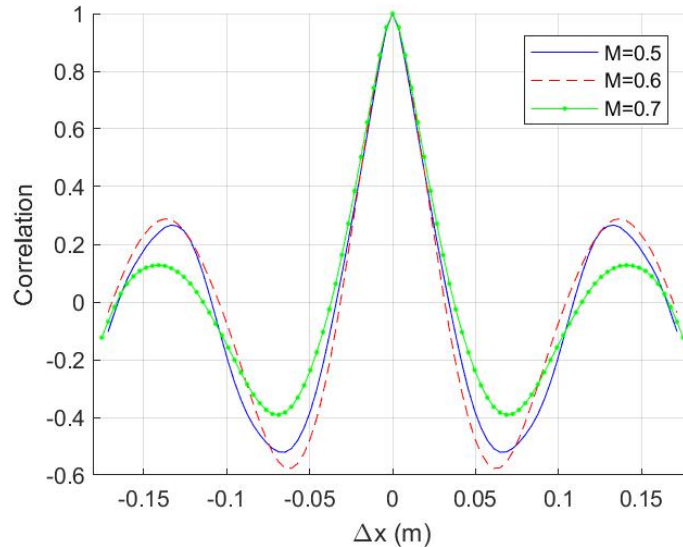


Figure 15. Normalized spatial correlations for different streamwise separation along the dashed-dotted line, indicated in Figure 14, for different incoming Mach numbers.

In Ref. 14, it was argued that the levels of aero-optical distortions due to the turbulent structures at subsonic speeds should be proportional to the freestream density, the freestream Mach number squared and the characteristic size of the optically-aberrating structure, $OPD_{rms} \sim \rho_{\infty} M_{\infty}^2 \Lambda$, the so-called “ ρM^2 ”-scaling. This scaling was demonstrated to be valid for subsonic turbulent boundary layers and turbulent flows around turrets at subsonic speeds below 0.6 [4,6,12]. To determine whether this scaling is applicable for the shear layers, aperture-averaged OPD_{RMS} values were computed from the flight data and plotted against $(\rho_{\infty} / \rho_{SL}) M_{\infty}^2 \Lambda$, as shown in Fig. 16. Note the shear layer related distortions are three times larger than the boundary layer related distortions, shown in Fig. 12, right. Indeed, the shear layer associated distortions approximately follow the “ ρM^2 ”-scaling for the $M = 0.5$ and 0.6 cases, with a proportionality constant of $A = 6.1$ ($\mu\text{m}/\text{m}$). However, at the highest Mach number case of 0.7 , the OPD_{RMS} value is slightly larger than the theoretical prediction. One possible explanation is that in development of the “ ρM^2 ”-scaling, it was assumed that all velocities are scaled with the freestream speed only. Consequently, the velocity ratio across the shear layer is assumed to be the same. At the transonic Mach number of 0.7 , the flow likely reaches a sonic speed; in other words, the flow chokes inside the holes of the porous fence. The choking forces the mass flow rate through the fence to be constant and therefore, results in the same Mach number downstream of fence regardless of the freestream transonic speed. This would lead to an increase of the shear layer velocity ratio causing the shear layer to thicken and the turbulence intensity inside of it to increase, resulting in additional aero-optical distortions [15,16].

If the shear layer exhibits self-similarity over the range of Mach numbers tested, the aperture-averaged spectra should collapse when normalized by $(\rho_{\infty} / \rho_{SL}) M_{\infty}^2 \Lambda$, and when frequency is converted to Strouhal number, St . Here, the Strouhal number is calculated based on the freestream velocity, U_{∞} and the structure size, Λ , giving the following, $St_{\Lambda} = f \Lambda / U_{\infty}$. These results are presented in Fig. 17. The wavefront spectra does exhibit reasonable collapse for frequencies above

$St_\Lambda = 0.1$. The sharp peaks near $St_\Lambda = 0.05$ are likely due to mechanical vibrations of the optical components. The wavefront spectra has a wide peak near $St_\Lambda^{(peak)} = 0.6$, which is indicative of the regular, convecting shear layer structures. The speed of these structures, U_c , can be calculated if the convective speed is assumed to be constant. As the shear layer structures are pseudo-periodic, the convective speed can be approximated by $U_C = f^{(peak)} \Lambda$. Substitution into the definition for St_Λ yields, $St_\Lambda^{(peak)} = f^{(peak)} \Lambda / U_\infty = U_C / U_\infty$. Thus from Fig. 16, the convective speed of the large-scale shear layer structures is approximately 0.6 of the freestream velocity, consistent with the convective speed measured in shear layers of similar velocity ratios [17].

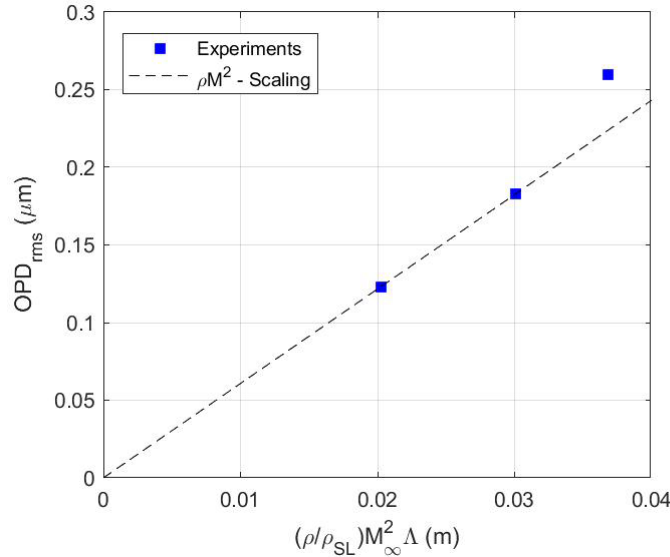


Figure 16. Shear layer aperture-averaged OPD_{rms} at different Mach numbers vs $(\rho_\infty / \rho_{SL})M_\infty^2 \Lambda$.

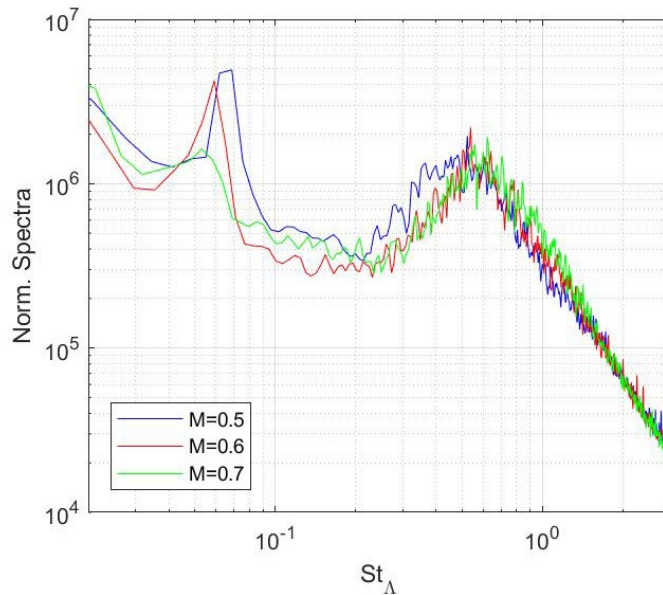


Figure 17. Shear layer aperture-averaged wavefront spectra, normalized by $(\rho_\infty / \rho_{SL})M_\infty^2 \Lambda$ as a function of $St_\Lambda = f \Lambda / U_\infty$ for different Mach numbers.

Finally, dispersion analysis was also performed on the shear layer wavefronts to independently verify the convective speeds and directions of various aero-optical components. The results for the dispersion analysis of the one-dimensional wavefront data at $M = 0.5$ are presented in Fig. 18. Here, the logarithm of the 2-D power spectrum is plotted to emphasize weaker components of the spectrum. The portion of the spectrum associated with the downstream convecting shear layer is located in the positive-frequency region, and circles indicate the locations of local spectral maxima. The black line, corresponding to the convective speed of $0.6U_\infty$, is plotted in the same region. For low wavenumbers ($k_x/(2\pi) < 30$ 1/m), the line agrees well with the spectrum's maxima and pertains to structures larger than 0.033 m. However, smaller structures corresponding to wavenumbers $k_x/(2\pi) > 30$ 1/m, appear to convect at a faster speed of $0.85 U_\infty$, as indicated by the red line in Fig. 18. The exact origin of these aero-optical distortions is not definitive at this time and additional investigation is necessary to address this question.

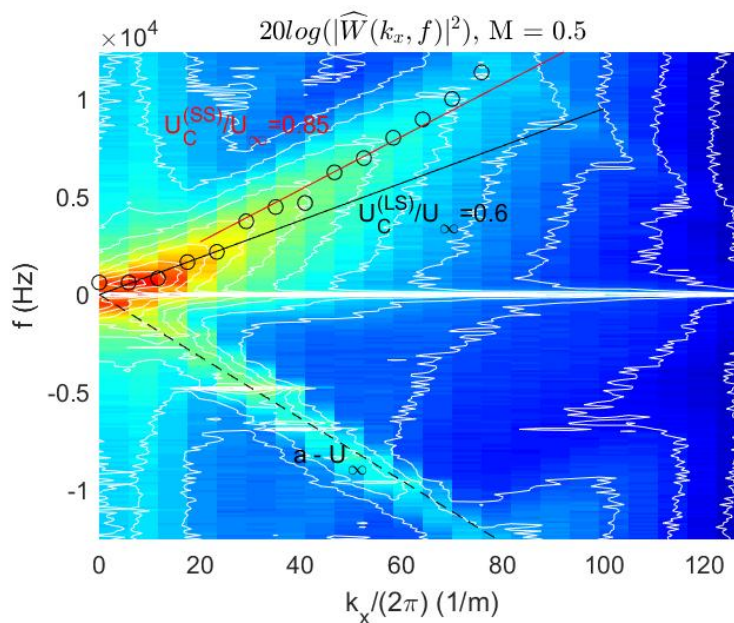


Figure 18. Two-dimensional Fourier transform, presented as $20 \cdot \log |\widehat{W}(k_x, f)|^2$ (in dB), for $M = 0.5$. Different convective speeds are indicated by solid and dashed lines. Contours (white lines) are separated by 5 dB.

While not observable in individual shear layer wavefronts shown in Fig. 14, the acoustical waves, prevalent in the boundary layer wavefronts, also exist in the shear layer data as seen in the negative-frequency region of Fig. 18. The dashed line represents the expected speed of these acoustically-related distortions, $a - U_\infty$, and agrees well with the spectrum slope in this region.

Fig. 19 shows the dispersion analysis of the one-dimensional wavefront data for the $M = 0.6$ and 0.7 cases. The shear-layer branch convecting at $0.6 U_\infty$, small-scale distortions traveling at $0.85 U_\infty$ and the acoustical distortions propagating upstream at a speed of $a - U_\infty$ are present at these Mach numbers.

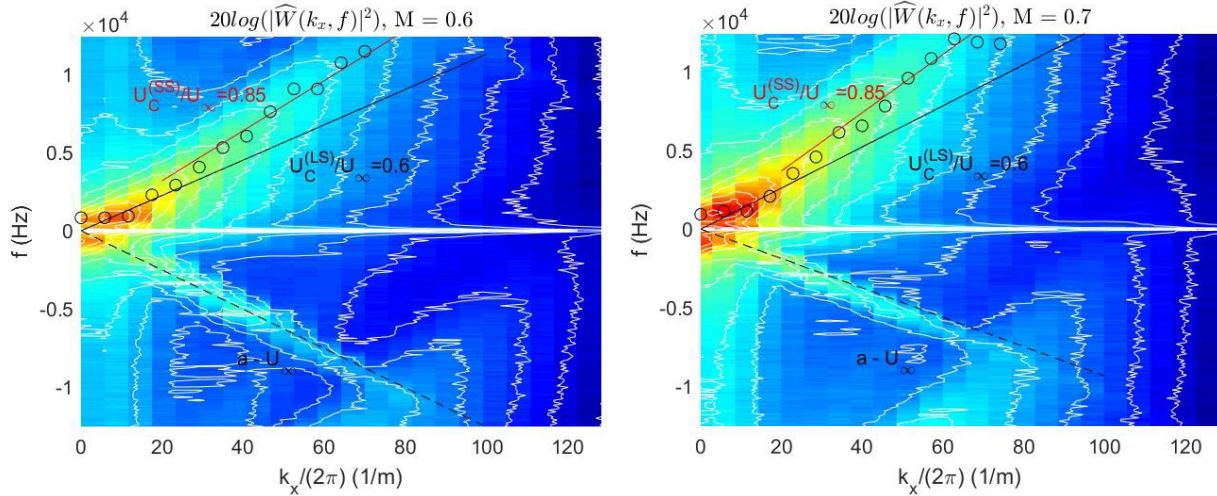


Figure 19. Two-dimensional Fourier transform, presented as $20 \cdot \log \left| \widehat{W}(k_x, f) \right|^2$ (in dB), for $M = 0.6$ (left plot) and $M = 0.7$ (right plot). Different convective speeds are indicated by solid and dashed lines. Contours (white lines) are separated by 5 dB.

V. Conclusions

Aero-optical distortions due to two fundamental flows, namely a boundary layer present over the fuselage of an aircraft and a shear layer formed by introducing a porous fence, were experimentally studied using AAOL-BC at different subsonic and transonic speeds. Additional tests were conducted to measure the boundary layer thickness over the location of the optical window. It was found that the boundary layer over AAOL-BC has non-uniform thickness over the window. This suggests that the boundary layer studied is not canonical, most likely due to the presence of a vortical structure which originates upstream in a cavity at the bottom of the cockpit window. Using POD and dispersion analysis, the acoustical component of optical aberrations due to the engine noise was dissociated from the overall aero-optical distortions and independently studied. It was found that the distortions due to engine noise is approximately constant over the range of Mach numbers studied. The aero-optical distortions due to the TBL were found to increase with the Mach number, consistent with the current model for the turbulent boundary layers. However, the amplitude of the aero-optical distortions caused by the TBL was found to be twice larger than theoretical predictions, further confirming a departure from a canonical description.

The shear layer introduced significantly larger aero-optical distortions due to the presence of large organized vortical structures. The aero-optical distortions were found to increase as flight Mach number squared, consistent with the existing model of aero-optical distortions. Using correlation and dispersion analysis, the size of the vortical structures was estimated, and their convective speed was found to be approximately 60% of the freestream velocity.

The presented results provide a quantitative description of various sources and corresponding aero-optical aberrations around a subsonic aircraft at varying cruise Mach numbers. The experimental results of optical distortions caused by realistic fundamental flows, such as boundary and shear layers are imperative to the design and implementation of airborne laser systems.

VI. Acknowledgments

This work is supported by the Joint Technology Office, Grant number FA9550-13-1-0001 and Office of Naval Research, Grant number N00014-18-1-2112. The U.S. Government is authorized

to reproduce and distribute reprints for governmental purposes notwithstanding any copyright notation thereon.

VII. References

- [1] Snyder, C.H., Franke, M.E., Masquelier, M.L., “Wind-Tunnel Tests of an Aircraft Turret Model”, *Journal of Aircraft*, 37(3), pp. 368-376, 2000.
- [2] Sluder, R., Gris, L., Katz, J., “Aerodynamics of a Generic Optical Turret”, *Journal of Aircraft*, 45(5), pp. 1814-1815, 2008.
- [3] Gordeyev, S., De Lucca, N., Jumper, E.J., Hird, K., Juliano, T.J., Gregory, J.W., Thordahl, J., and Wittich, D.J., “Comparison of Unsteady Pressure Fields on Turrets with Different Surface Features using Pressure Sensitive Paint”, *Experiments in Fluids*, 55, p. 1661, 2014.
- [4] Porter C., Gordeyev, S., Zenk, M. and Jumper, E.J., "Flight Measurements of the Aero-Optical Environment around a Flat-Windowed Turret", *AIAA Journal*, 51(6), pp. 1394-1403, 2013.
- [5] De Lucca, N., Gordeyev, S., and Jumper, E.J., "In-flight aero-optics of turrets", *Journal of Optical Engineering*, 52(7), 071405, 2013
- [6] J. Morrida, S. Gordeyev, N. De Lucca, E.J. Jumper, " Shock-Related Effects on Aero-Optical Environment for Hemisphere-On-Cylinder Turrets at Transonic Speeds ", *Applied Optics*, 56(16), pp. 4814-4824, 2017.
- [7] N. De Lucca, S. Gordeyev, E. Jumper and D.J. Wittich, "Effects of engine acoustic waves on optical environment around turrets in-flight on AAOL-T", *Optical Engineering*, 57(6), 064107, June 2018.
- [8] Jumper, E.J., Zenk, M., Gordeyev, S., Cavalieri, D., and Whiteley, M., "Airborne Aero-Optics Laboratory", *Journal of Optical Engineering*, 52(7), 071408, 2013.
- [9] E.J. Jumper, S. Gordeyev, D. Cavalieri, P. Rollins, M.R. Whiteley and M.J. Krizo , “Airborne Aero-Optics Laboratory - Transonic (AAOL-T) ”, *AIAA Paper 2015-0675*, 2015.
- [10] S. Gordeyev, W.R. Burns, E. Jumper, S. Gogineni, M. Paul and D.J. Wittich, "Aero-Optical Mitigation of Shocks Around Turrets at Transonic Speeds Using Passive Flow Control ", *AIAA Paper 2013-0717*, 2013.
- [11] K. Taira, et al., “Modal Analysis of Fluid Flows: An Overview,” *AIAA Journal*, Vol. 55, No.12, Dec. 2017.
- [12] S. Gordeyev, A. E. Smith, J.A. Cress and E.J. Jumper, " Experimental studies of aero-optical properties of subsonic turbulent boundary layers", *Journal of Fluid Mechanics*, 740, pp. 214-253, 2014.
- [13] Fitzgerald EJ, Jumper EJ. “The optical distortion mechanism in a nearly incompressible free shear layer”, *J. Fluid Mech.* 512, pp. 153–89, 2004.
- [14] Gordeyev, S., and Jumper, E.J., “Fluid Dynamics and Aero-Optics of Turrets”, *Progress in Aerospace Sciences*, 46, pp. 388-400, 2010.
- [15] Brown, G. L. and Roshko, A,”On density effects and large structure in turbulent mixing layers”, *J. Fluid Mech.* 64, pp. 775-816. 1974.
- [16] Rogers, M. M. and Moser, R. D.,”Direct simulation of a self-similar turbulent mixing layer”, *Phys. Fluids*, 6, pp. 903-923, 1994.
- [17] D.A. Duffin, ”Feed-forward adaptive-optic correction of a weakly-compressible high-subsonic shear layer”, Ph. D. Thesis, University of Notre Dame, 2009; P. M. Ranade, “Turbulence amplitude modulation in an externally forced, high Reynolds number boundary layer”, Ph. D. Thesis, University of Notre Dame, 2016.